PCCP

Accepted Manuscript

ROYAL SOCIETY OF CHEMISTRY

www.rsc.org/pccp

Journal Name

ARTICLE

Structural, Optical and Photoelectrochemical Characterizations of Monoclinic Ta_3N_5 Thin Films†

Received 00th January 20xx,
Accepted 00th January 20xx

DOI: 10.1039/x0xx00000x

www.rsc.org/

Sherdil Khan,[a] Maximiliano J. M. Zapata,[a] Marcelo B. Pereira,[a] Renato V. Gonçalves,[b] Lukas Strizik,[d] Jairton Dupont,[e] Marcos J. L. Santos,[c] and Sérgio R. Teixeira[a*]

Monoclinic Ta_3N_5 thin films were synthesized by thermal nitridation of amorphous Ta_2O_5 films directly sputtered by radio frequency magnetron sputtering. The samples were studied by high resolution transmission electron microscopy, X-ray photoelectron spectroscopy, UV-Vis-NIR spectrophotometry, Rietveld refinements, spectroscopic ellipsometry and electrochemical techniques. The surface composition of Ta_3N_5 thin film was found different than the underlying film, affecting the optical properties of the material. The Rietveld refinement has confirmed that nitridation process results in Schottky and oxygen substitutional defects within the crystalline structure of monoclinic Ta_3N_5 thin film. The optical constants of the film were obtained by spectroscopic ellipsometry within a spectral range of 4.60–0.54 eV, i.e. 270–2 300 nm. The suitable parameterization was found to consist of three Tauc-Lorentz and one Lorentz oscillators. The conduction band, valence band and the flat band positions were determined by photoelectrochemical techniques, presenting a strong dependence on pH of the eletrolyte. Improved photocurrent was obtained in alkaline condition and attributed to the shorter depletion region width measured by Mott-Schottky and the lower recombination life time measured by open circuit potential decay analyses.

Introduction

In recent years, Ta_3N_5 has emerged as a promising candidate for photoelectrochemical (PEC) water splitting.[1,2,3] Compared to other semiconductors as TiO_2 and hematite, the use of Ta_3N_5 for water splitting is relatively new and further investigations are required to better understand its physicochemical properties and to improve its photocatalytic performance.[4,5,6-7] Usually, Ta_3N_5 is prepared by thermal nitridation of Ta_2O_5 under NH_3 environment.[8,9] The literature reports that Ta_3N_5 presents two different crystalline phases, monoclinic (JCPDS file 89-5200) and orthorhombic (JCPDS file 79-1533). The diffraction patterns of these phases resemble each other since their lattice parameters are almost the same; therefore, a special attention is necessary to assign the corresponding crystalline phases of Ta_3N_5. The easiest approach to assign any of these phases from the XRD patterns is to observe the difference in relative intensity between 2θ peaks of 24.5° and 31.4° once for monoclinic Ta_3N_5 the intensity of peak 24.5° is higher than the 31.4°.[10] The crystalline phases of Ta_3N_5, largely depend on the route of synthesis and the choice of precursor and substrate.[11] The orthorhombic phase of Ta_3N_5 has been widely reported, but there are few reports on monoclinic phase.[12,13] Several works in the literature show that oxygen is a natural impurity in the Ta_3N_5 lattice. The oxygen improves mechanical, structural and cohesion properties; however the location of oxygen in the unit cell for monoclinic Ta_3N_5 is not discussed.[14,15] In addition, excessive oxygen content may introduce recombination centers for photogenerated carriers. Therefore, for PEC applications the oxygen content should be considered carefully.[3,16]

Semiconducting thin films have been widely investigated to study their physicochemical properties once they are easy to model,[17,18,19] In order to synthesize thin films various preparation methods have been reported.[20,21] Recently, magnetron sputtering has attracted considerable attention as a clean technique to synthesize thin films.[22,23] In the literature, the Ta films have been sputtered on a substrate that were post-annealed to form Ta_2O_5 and consequently nitrided to transform Ta_3N_5.[24] In addition, Ta_3N_5 thin films have been reactively sputtered from Ta target using a mixture of Ar-N_2-O_2 as working gas and post-nitrided to improve the crystallinity.[15,25] Direct sputtering of Ta_2O_5 for its transformation to Ta_3N_5 by thermal nitridation is an attractive option for the synthesis.

Concerning the PEC applications of monoclinic Ta_3N_5 thin films, the determination of the effective donor density (N_D) and the depletion layer width (W) is crucial for understanding semiconductors/liquid interfaces.[26,27] In order to obtain these

[a] Institute of Physics, Universidade Federal do Rio Grande do Sul, Av Bento Goncalves 9500 POBox - 15051 91501-970, POA-RS, Brazil
[b] Instituto de Física de São Carlos, Universidade de São Paulo, CP 369, São Carlos 13560–970, SP, Brazil.
[c] Institute of Chemistry, Universidade Federal do Rio Grande do Sul, Av Bento Goncalves 9500, POA-RS, Brazil.
[d] Department of General and Inorganic Chemistry, Faculty of Chemical Technology, University of Pardubice, Studentska 573, 53210, Pardubice, Czech Republic.
[e] School of Chemistry, University of Nottingham, University Park, Nottingham, NG7 2RD, United Kingdom.
* srgrbrtxr@gmail.com

† Electronic Supplementary Information (ESI) available: [Figures and tables]. See DOI: 10.1039/x0xx00000x

parameters from the Mott-Shottky analyses, the knowledge of the dielectric constant is necessary and spectroscopic ellipsometry (SE) has been found to be a powerful tool to determine it.[28,29] The positions of the valence band maximum (VBM), conduction band minimum (CBM) and the flat band potential (V_{fb}) are of fundamental importance for PEC applications, influencing water splitting activity.[30] For overall water splitting the water redox potentials must be straddled within the material bandgap. Hence, understanding the band structure of monoclinic Ta_3N_5 thin films prepared from directly sputtered Ta_2O_5 thin films is of great interest.

In this work, thin films of Ta_2O_5 have been directly sputtered from Ta_2O_5 target by radio frequency (RF) magnetron sputtering and afterwards thermally nitrided to obtain monoclinic Ta_3N_5 thin films. Surface, structural, optical and PEC analyses are provided to understand the physico-chemical properties of the film.

Results and discussion

Surface composition and structure

The SEM images of the films are shown in Fig.1. As-sputtered Ta_2O_5 film presents a smooth, homogenous and flat surface (Fig. 1a). However, after nitridation, some patches appeared on the entire surface (Fig. 1b). The diameters of these patches were calculated by estimating the average of longest and shortest distance inside each patch, that was ~10.4 µm and the average spacing between them was approximately ~24 nm. The patches observed in films at higher temperature are attributed to the interfacial stress caused by the difference in thermal expansion of the film and the substrate.[31] To further investigate the grain size and crystallinity of the sample; HRTEM images were obtained from the patch surface. Fig. 1c shows a crystalline grain with an approximated size of ~ 46 nm. In addition, at the grain boundary one can observe some amorphism which might be related to the oxygen segregation during the nitridation. The interplanar spacing of 0.512 nm is in agreement with (200) plane of monoclinic Ta_3N_5 (Fig. 1d). Furthermore, polycrystalline monoclinic Ta_3N_5 can be confirmed by selected area electron diffraction (SAED) patterns shown in Fig. S2†. Fig. 2 compares the XPS spectra of the samples. From the survey spectra of as-sputtered Ta_2O_5 thin film one can observe comparably large amount of oxygen. The nitridation has decreased oxygen content, as expected, as a result of nitrogen incorporation in the lattice (Fig. 2b). However, after sputter etching the Ta_3N_5 film, the oxygen content is further decreased; but not completely eliminated (Fig. 2c). The positions of O1s and N1s peaks are marked in the survey spectra. To further investigate the surface of the monoclinic Ta_3N_5 thin film, Ta4f and N1s regions were obtained in high resolution. $Ta4f_{7/2}$ and $Ta4f_{5/2}$ are positioned at 26.5 and 28.4 eV, respectively; for as-sputtered Ta_2O_5 thin film (Fig. 2d). For as-nitrided Ta_3N_5 thin film (Fig. 2e) the core lines of $Ta4f_{7/2}$ and $Ta4f_{5/2}$ are centered at 25.3 and 27.2 eV, respectively; with a spin orbital separation of 1.9 eV. Comparing to the literature, these binding energies are similar to tantalum oxynitride species.[32]

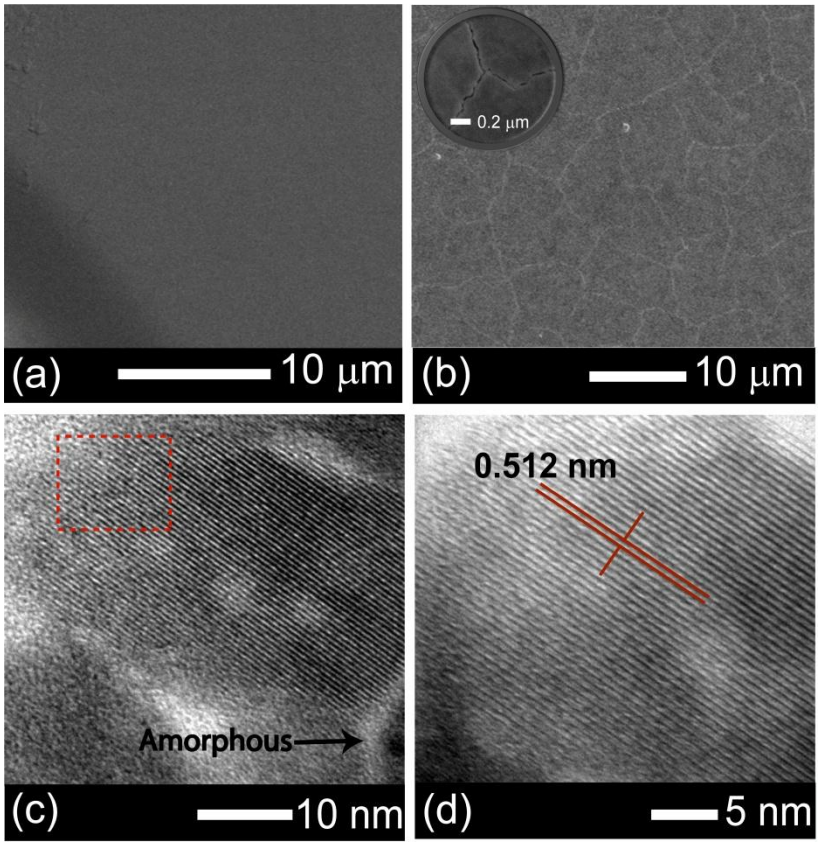

Fig. 1 SEM images of (a) as-deposited Ta_2O_5, (b) as-nitrided Ta_3N_5 thin films. (c) and (d) HRTEM image of Ta_3N_5 thin films.

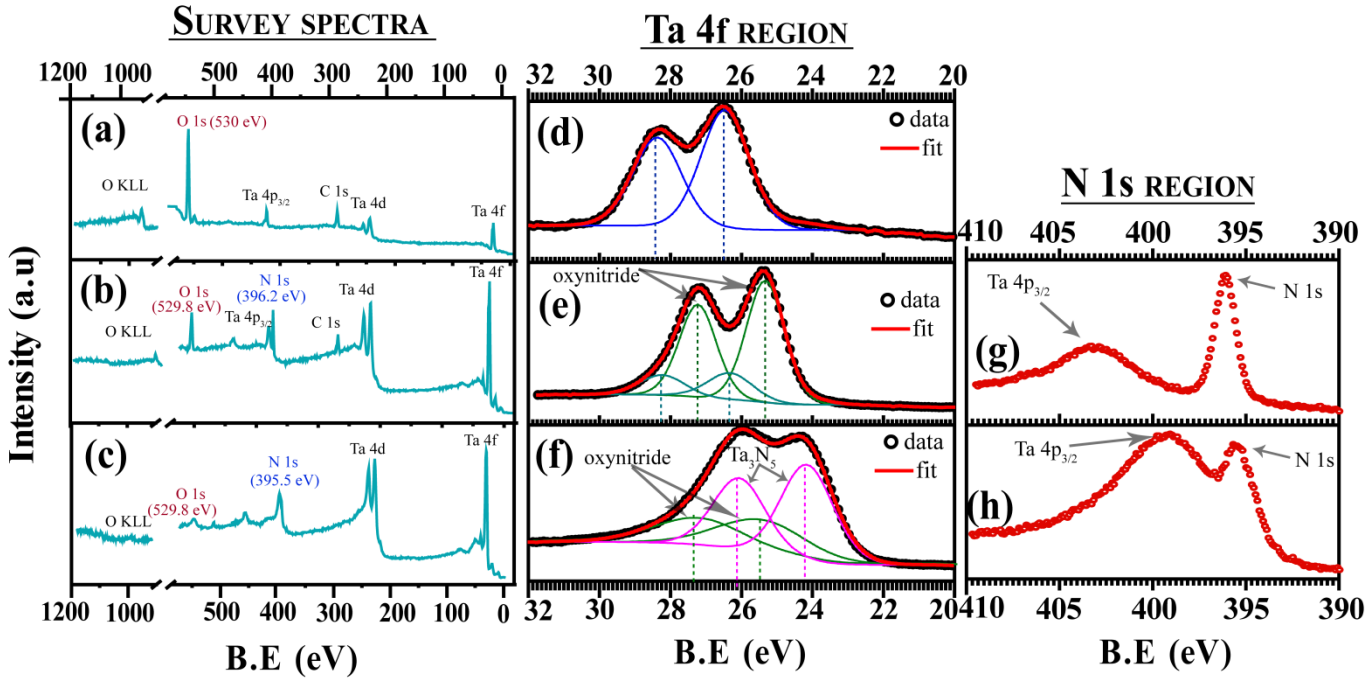

Fig. 2 XPS survey spectra of (a) as-sputtered Ta_2O_5 thin film , (b) Ta_3N_5 thin films before sputter etching, (c) Ta_3N_5 thin films after sputter etching, (d) Ta4f region spectra of as-sputtered Ta_2O_5 thin film, (e) Ta_3N_5 thin films before sputter etching, (f) Ta_3N_5 thin films after sputter etching, (g) N1s region spectra of Ta_3N_5 thin films before (h) N1s region spectra of Ta_3N_5 thin films after sputter etching.

In addition, high-energy-side small doublet was also detected; suggesting the presence of low energy states (Ta^{4+}, Ta^{3+}) of Ta.[33,34] The formation of reduced tantalum species in Ta_3N_5 obtained by thermal nitridation, has been reported earlier. [35, 36] The Ta4f spectrum of Ta_3N_5 thin film after sputter etching (Fig. 2f) clearly differs in shape when compared to the Ta4f regions of Fig. 2d and 2e and is shifted toward lower binding energy. The core lines are centered at 24.3 and 26.2 eV; corresponding to Ta_3N_5. In addition, a high-energy-sided small doublet is observed at the same binding energy of oxynitride species of Ta shown in Fig. 2e. After sputter etching, the concentration of oxynitride species is decreased. Furthermore, the N1s spectrum shown in Fig. 2h presents a wide peak of Ta $4p_{3/2}$ which is strongly overlapped with the N1s, however as shown in Fig. 2g the Ta$4p_{3/2}$ is distinctive. In addition, the binding energy of N1s shown in Fig. 2h is shifted to a lower value as compared to the N1s of Fig. 2g. The strong overlapping of Ta $4p_{3/2}$ and the change in the binding energy position of N1s clearly indicate the presence of two different species on the surface of the film. These results strongly suggest a different composition of the surface and the underlying film. The top surface of as-nitrided thin film is mainly composed of oxynitride species. Recently, *Nurlaela et al* have shown the presence of species such as TaN on the top surface of Ta_3N_5 particles. The authors have shown that cleaning the surface improves the photocatalytic activity.[37] The results obtained by XPS and HRTEM, clearly show that Ta_3N_5 surface should be carefully considered for photocatalytic water splitting applications. The presence of these oxynitride species and the amorphous layer around the grain can act as recombination centers for photogenerated carriers. Nevertheless, the different chemical composition of the surface can affect the optical properties of the film.

The XRD patterns of the synthesized films are shown in Fig. 3a. It can be seen that Ta_2O_5 thin films are amorphous. However, after nitridation at 900°C for 24h clear changes in the patterns can be observed. The amorphous Ta_2O_5 is transformed to crystalline Ta_3N_5. All peaks observed in the XRD diffractograms are in good agreement with the monoclinic phase of Ta_3N_5 (JCPDS file 89-5200) with preferential orientation along (110).[38] To understand the crystalline structure of Ta_3N_5 thin films, Rietveld refinement was performed (Fig. S3†). From the analysis of the Rietveld refinement, the grain size along different directions was calculated (Table, S1†). The average grain size was approximated to 40 nm corroborating the size calculated by the HRTEM (Fig. 1c). The unit cell obtained by the refinement is shown in Fig. 3b. The Schottky defects of tantalum and nitrogen are observed at the Wyckoff positions Ta1 (4i) and N1 (4i) (Fig. 3b) presenting 0.82 and 3.05% of vacancies, respectively (Table. S2†). However, other sites are completely filled. The stoichiometric Ta_3N_5 model used for the refinement has yielded reasonable fits and by considering a mixed of Schottky defects of nitrogen with substitutional oxygen an improved refinement was obtained. According to the occupancy factor of refinement, the Wyckoff positions with higher oxygen sharing probability were observed for 3-coordianted N Wyckoff sites namely N2 (4i) and N3 (4i) which are substituted by O1 and O2, respectively. For N2 (4i) and N3 (4i) sites the oxygen substitutions were 1.28 and 9.05% respectively and the remaining of these Wyckoff sites are completed with nitrogen (Table S2†). The sites at which oxygen sharing are more probable are marked in red (Fig. 3b). Interestingly, the results obtained in this work for monoclinic Ta_3N_5 match with the orthorhombic Ta_3N_5 showing the same tendency of oxygen incorporation for 3-coordinated N atoms.[13]

Journal Name

ARTICLE

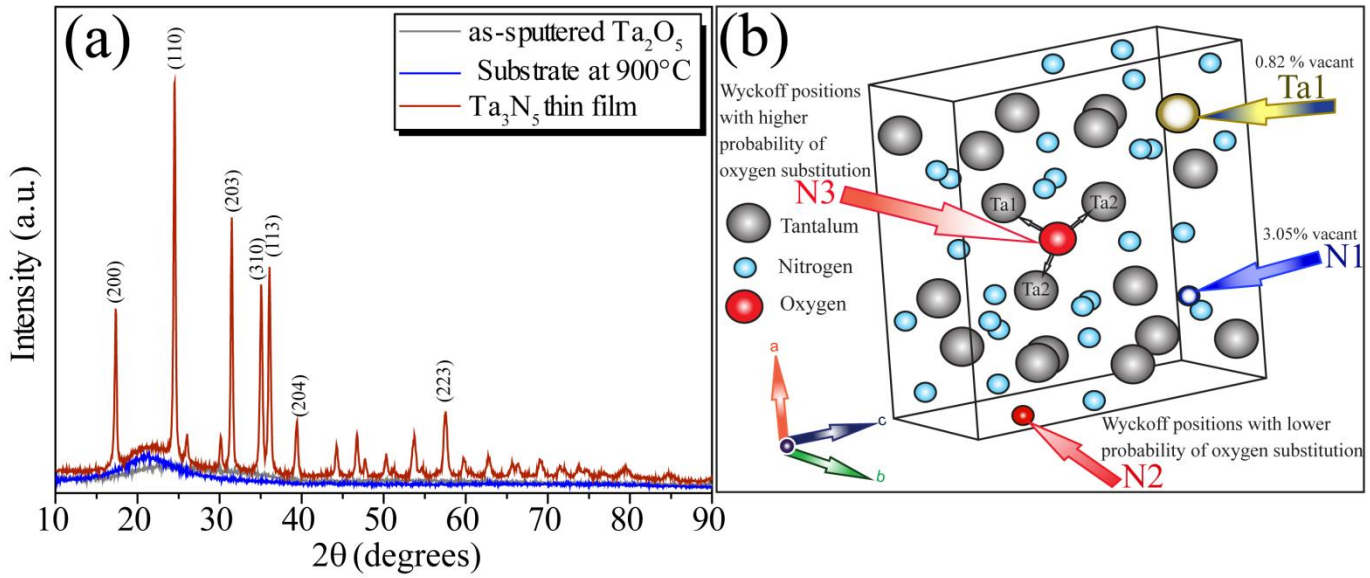

Fig. 3 (a) XRD patterns for Ta_2O_5, the substrate nitrided at 900°C and Ta_3N_5 thin films obtained after nitridation. (b) Unit cell of monoclinic Ta_3N_5 thin film.

Comparing the bond distances for the substitutional oxygen sites has provided an interesting result; when oxygen O1 substitutes N2 (bonded with Ta1) a decrease in interatomic distance of 8.08% (Ta1-N2 (2.1670 Å) > Ta1-O1 (1.9918 Å)) was observed. On the other hand, for N2 bonded with Ta3 an increase of 21% was recorded for O1 substitution (Ta3-N2 (1.3531 Å) > Ta3-O1 (2.9962 Å)). Furthermore, the substitution of N3 with O2 results in an increase of interatomic distance of 14.34% (Ta2-N3 (2.1685 Å) < Ta2-O2 (1.8035 Å)). Therefore, substitutional oxygen produces lattice deformation. In previous theoretical studies on the oxygen doping of Ta_3N_5 the presence of oxygen has shown to improve mechanical and adhesion properties as well as decreased the value of dielectric constant of Ta_3N_5.[14,16] We may suggest that the lattice deformation due to the oxygen substitution can be related to these phenomena. Based on the occupancy/vacancy concentrations displayed in Table S2† the nominal stoichiometry was obtained as $\mathbf{Ta_{2.990}N_{4.867}O_{0.133}}$. This result clearly shows that oxygen cannot be completely removed even under harsh nitridation temperatures, such as 900°C for 24h.

Optical properties

The surface and structural analyses discussed above have highlighted the complexity of monoclinic Ta_3N_5 thin films. The structural composition of the Ta_3N_5 surface (top layer) is proven to be different that the underlying film. This top layer must be taken into account for the derivation of suitable SE model and to find correct optical constants. Generally, the ellipsometry parameters Ψ and Δ are related to the complex pseudo-dielectric function $\langle\varepsilon\rangle$ by:[39]

$$\langle\varepsilon\rangle = \langle\varepsilon_1\rangle + i\langle\varepsilon_2\rangle = \varepsilon_a\left[\left(\frac{1-\rho}{1+\rho}\right)\sin^2\phi + \cos^2\phi\right]\tan^2\phi \qquad (1.4)$$

where $\langle\varepsilon_1\rangle$ *and* $\langle\varepsilon_2\rangle$ are the real and the imaginary parts of the complex pseudo-dielectric function, ϕ is the angle of light incidence, ε_a is dielectric function of the ambient and the ellipsometric ratio ρ = tan(Ψ) exp($i\Delta$). The complex pseudo-dielectric function is equal to the complex dielectric function of the material under study, only when the material is opaque or has a semi-infinite thickness. Furthermore, the material does not contain any top layer, e.g. roughness, oxide etc.[40] Usually, in materials (especially semiconductors and metals) including Ta_3N_5 thin films, these conditions do not meet completely. In such materials the surface can be affected by the oxidation process and/or by the surface roughness leading to different optical constants of the top layer and the underlying film.[36,37] Based on the semiconductor nature of monoclinic Ta_3N_5 thin films, suitable parameterization for derivation of the dielectric functions can be a combination of Tauc-Lorentz and Lorentz oscillators described below.[41,42] The imaginary part of the dielectric function ε_{2TL} using the Tauc-Lorentz oscillator is a product of Tauc joint density of states (when $E > E_g$) and Lorentz model:

$$\varepsilon_{2TL} = \begin{cases} \dfrac{A_o E_o C_o (E-E_g)^2}{(E^2-E_o^2)^2 + C_o^2 E^2}\dfrac{1}{E} & when\ E > E_g, \\ 0 & when\ E \le E_g, \end{cases} \qquad (1.5)$$

where A_o, C_o, E_o *and* E_g are the amplitude (oscillator strength), peak broadening, peak transition energy and optical bandgap energy, respectively. Furthermore, the real part of the dielectric function ε_{1TL} is calculated from the imaginary part ε_{2TL} using the Kramers-Kronig relation:[43,44]

$$\varepsilon_{1TL} = \varepsilon_1(\infty) + \frac{2}{\pi} P \int_{E_g}^{\infty} \frac{\xi \varepsilon_{2TL}(\xi)}{\xi^2 - E^2} d\xi, \quad (1.6)$$

where $\varepsilon_1(\infty)$ is a fitting parameter giving the constant contribution to ε_{1TL} at higher photon energies, P is the Cauchy principal part of the integral. The complex dielectric function ε_L can be expressed in Lorentz parameterization as:[45]

$$\varepsilon_L = \frac{A_o E_o}{E_o^2 - E^2 - iC_o E}. \quad (1.7)$$

To parameterize the monoclinic Ta_3N_5 film, firstly; the thickness of the film was fixed to a value of 893 nm known from profilometry (Fig. S4†). The indirect bandgap[46] was determined from extrapolation of linear part in the $(\alpha E)^{1/2}$ versus E plot (Fig. 4); resulting an approximate value of optical band gap energy Eg ~ 2.0 eV.

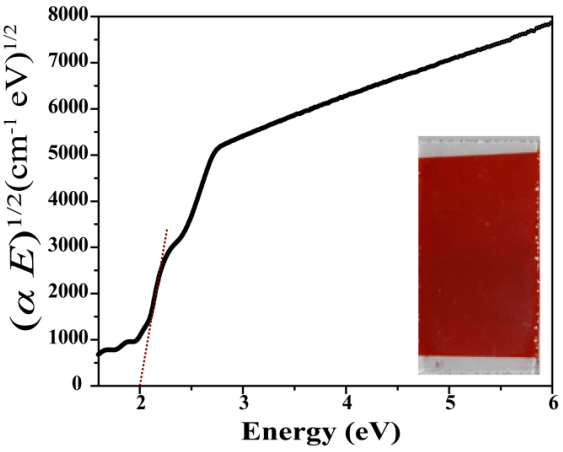

Fig. 4 Determination of indirect bandgap of monoclinic Ta_3N_5 thin film. The α values are obtained from equation 1.3 (Experimental section).

As discussed earlier in the XPS analyses; the top layer of the film presents a different chemical composition than the underlying Ta3N5 thin film. Therefore, we used various parameterization models to find the optical constants of the material. We used the effective medium approximation according to Bruggeman which is composed of Ta3N5 and voids (in volume of the material as well as on its surface representing material roughness). However, in this case high MSE value was obtained. On the other hand, when refractive index gradation of the studied film was assumed, the MSE was significantly decreased to MSE ≈ 8. In Fig. 5 the gradation is shown at E = 0.8 eV with variations of the dielectric constant ε_1 from 6.0 (bottom) to 6.7 (top). The gradation consists of two layers that fully reflects the difference between the top layer and the underlying Ta_3N_5 film. These results suggest that the optical properties of the surface are different and considering refractive index gradation to parameterize SE data is physically true.

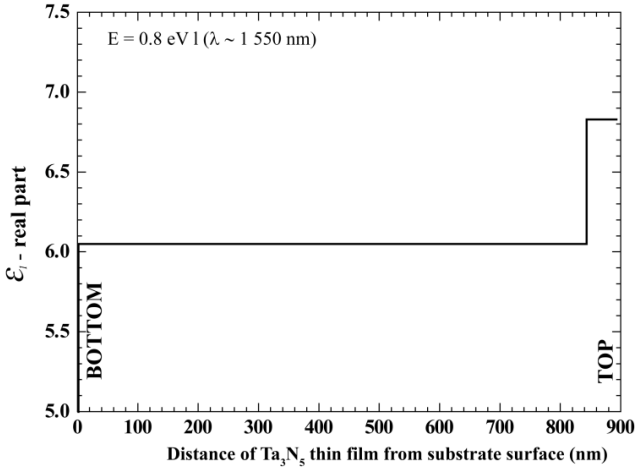

Fig. 5. Gradation of the real part of dielectric constant ε_1 at photon energy E = 0.8 eV in monoclinic Ta_3N_5 thin film obtained by spectroscopic ellipsometry.

The aforementioned procedure was used as a start point for direct inversion of experimental data by "Point-by-point" fit that allowed obtaining both real ε_1 and imaginary ε_2 parts of dielectric constants related to monoclinic Ta_3N_5. However, these functions are not Kramers-Kronig consistent. Hence, the parameterization model for spectral region from 0.54 to 4.60 eV was carried out. We used three Tauc-Lorentz (*TL*) oscillators and one Lorentz (*L*) oscillator as suitable parameterization as discussed in the previous reports.[40,41]

Table 1 The SE parameters of optical model based on four oscillators for Ta_3N_5 film.*

Oscillator	A_o/eV	C_o/eV	E_o/eV	E_g/eV
TL1	75 ± 2	1.14 ± 0.04	2.00 ± 0.01	2.0 (fixed)
TL2	294 ± 6	1.05 ± 0.03	3.254 ± 0.008	3.017 ± 0.003
TL3	162 ±12	4.0 ± 0.4	4.51 ± 0.05	3.60 ± 0.04
L1	1.64 ± 0.02	0.526 ± 0.006	3.101 ± 0.005	–

** TL and L denote the Tauc-Lorentz oscillator and Lorentz oscillator, respectively. $\varepsilon_1(\infty)$ =0.69±0.10 and MSE = 7.7.*

To describe more precisely the absorption edge around ~2 eV the Lorentz oscillator *L*1 was used in combination with Tauc-Lorentz oscillator *TL*1 (Table 1). The refractive index gradation (Fig. 5), thickness of the film obtained by profilometry (893 nm) and the optical bandgap energy of one Tauc-Lorentz *TL*1 oscillator (E_g = 2.0 eV) were set to be fixed parameters. The fixed optical bandgap energy E_g value of the *TL*1 oscillator is in accordance with the *Tauc´s* plots of Fig. 4. where E_g was evaluated to be ≈ 2.0 eV. Using this model, the fit of Ψ and Δ experimental data is shown in the Fig. S5 with a resulting **MSE of 7.7** which is reasonable value in comparison with previously reported **MSE of 8.5**.[41] The obtained dielectric constants for Ta_3N_5 thin film with resulting oscillators used for fits are presented in Fig. 6a. In the visible spectral region i.e. the wavelength window for photoelectrochemical water splitting applications (3.1–1.7 eV) the dielectric function ε_1 of monoclinic Ta_3N_5 film was in the range of 7–9. These values

are in agreement with the theoretically reported value for Ta_3N_5.[16] At the same spectral range the dielectric function ε_1 of top layer was in a range of 8–10 and (Fig. S6†).

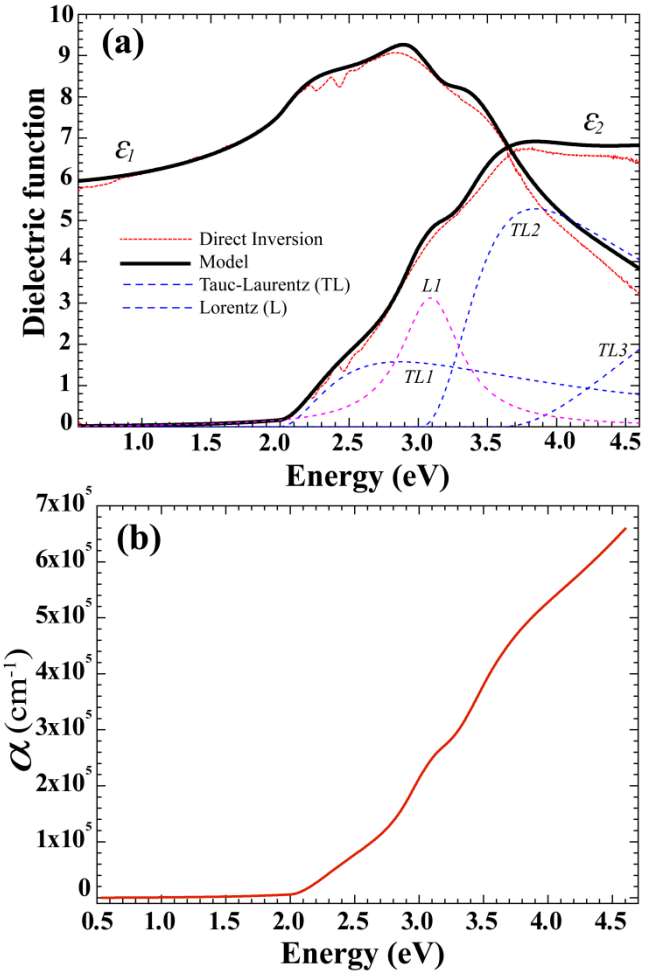

Fig. 6 (a) Real ε_1 and imaginary ε_2 parts of dielectric functions of monoclinic Ta_3N_5 film directly inverted (red dotted lines) and modelled (black solid lines) by set of Tauc-Lorentz and Lorentz oscillators (blue and magenta dashed lines) from SE experimental data. (b) Absorption coefficient α of the Ta_3N_5 film obtained from optical model of the fitted SE data.

The validity of the model used here can be confirmed from Fig. S7† where the experimentally measured transmittance matches the transmittance obtained by the parameterization of the SE data. These results clearly indicate that the SE is a powerful tool to measure the dielectric constants of a given material. According to the Beer-Lambert law, the absorption coefficient α of a material is related to the extinction coefficient $k(\lambda)$ by the following equation:

$$\alpha = \frac{4\pi k}{\lambda} \quad (1.8)$$

The absorption coefficient α (cm^{-1}) obtained by equation 1.8 from the actual parameterization model of SE data is shown in Fig. 6b. In the visible spectral region the absorption coefficient of monoclinic Ta_3N_5 film varies from $\alpha \approx 2.5 \times 10^5$ cm^{-1} (at E = 3.1 eV) to $\alpha \approx 3 \times 10^3$ cm^{-1} (at E = 1.7 eV).

PEC properties of monoclinicTa_3N_5 thin films

The bandgap energy of Ta_3N_5 overcomes the endothermic 1.23 eV requirement for the water splitting.[16] However, the positions of valence band maximum (VBM) and conduction band minimum (CBM) relative to the water redox potentials shall be taken into account. Firstly, we have determined the position of the VBM by anodic scan under dark.[2] For an n-type semiconductor under dark, the reverse biasing induces more band bending. The increase in the biasing to a certain potential leads to extreme depletion or carrier inversion once the Fermi level energy is positive with respect to the valence band energy.[30,48] At this moment, the current flowing across the interface is irreproducible and likely to be dominated by the tunnelling process through the Helmholtz layer.[48] The onset of that process yields the VBM.[2] Fig. 7 (top) compares the linear sweep voltammetry (LSV) curves of the samples, under dark, as a function of pH. We scanned the potentials from the open circuit potential (V_{oc}) to the anodic onset. It can be seen that by increasing the pH of the electrolyte the VBM shifts negatively (Table 2). An additional benefit along with obtaining the position of VBM from the anodic scans is the identification of the potentials for the non-faradic processes i.e the Mott-Schottky window where all applied potential is dropped across the semiconductor rather the Helmholtz layer. The capacitance of the Helmholtz layer is fairly greater than the capacitance of the semiconductor and at these conditions the system exhibits depletion state. Therefore, in this potential window the Mott-Schottky approximation is valid to measure the flat band of the semiconductor. A section of the Mott-Schottky window is highlighted in Fig. 7 (top) for each electrolyte. In the Mott-Schottky equation: [49]

$$\frac{1}{C^2} = \frac{2}{\varepsilon_1 \varepsilon_0 A^2 e N_D}\left(V - V_{fb} - \frac{K_b T}{e}\right) \quad (1.9)$$

C, e, ε_1, ε_0, V, k_B and V_f are the space charge capacitance, elementary electron charge, dielectric constant of Ta_3N_5 (**Fig. 6a**), vacuum permittivity, applied potential, Boltzmann constant and the flat band potential, respectively. Fig. 7 (bottom) compares the Mott-Schottky plots of the Ta_3N_5 thin films measured in each electrolyte. The obtained values of V_f and N_D are presented in Table 2. As observed for VBM, the V_f also shifts negatively with increasing pH. However, the donor density is significantly increased from pH 4 to pH 12 that is clearly related to the changing composition of Ta_3N_5/solution interface with respect to the species in solution. In essence, Ta lattice sites are Lewis acid sites allowing the adsorption of hydroxyl ions, whereas the oxygen and nitrogen lattice sites are Lewis base sites capturing protons. The oxygen and nitrogen sites exhibit different reactivity to the proton attachment[50] therefore, the effective donor density strongly depends on the pH of the electrolyte for monoclinic Ta_3N_5 thin films.

To investigate the PEC performance and further study the flat band potential of Ta_3N_5 thin films by photocurrent onset, chopped linear sweep voltammetry (LSV) measurements were performed (Fig. 8).

Journal Name

ARTICLE

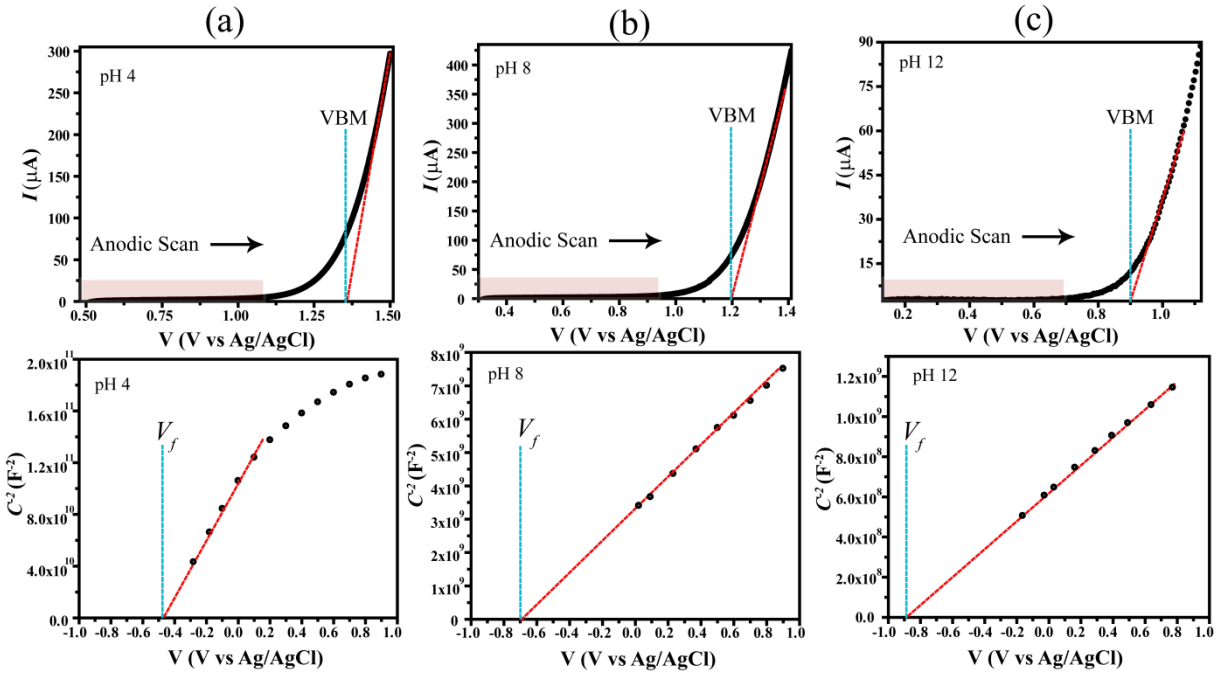

Fig. 7 LSV curves (top) and Mott-Schottky plots (bottom) of Ta_3N_5 thins films obtained in 0.1 M phosphate buffer solutions adjusted to pH (a) 4, (b) 8 and (c) 12.

Table 2 (Photo)electrochemical parameters deduced from LSV curves, Mott-Schottky plots and open circuit potential decay measurements.

pH	V_{oc}/V	$^{O}V_{oc}$/V	V_f/V	N_D/cm^{-3}	W/nm	CBM/V*	VBM/V
4	0.48	0.25	−.46	1.2 ×10^{18}	24.62	−0.71/**−.28**	1.38/**1.81**
8	0.25	0.01	−.70	5.1 ×10^{19}	04.25	−0.95/**−.28**	1.17/**1.84**
12	0.04	-0.20	−.89	1.3 ×10^{20}	02.91	−1.14/**−.23**	0.92/**1.83**

*$^{O}V_{oc}$ obtained under illumination (1 Sun). * The bold and underlined Potentials are converted to RHE.*

The electrolyte at pH 12 presents enhanced photocurrent compared to pHs 4 and 8, that can be rationalized from the Mott-Schottky analyses, as the N_D has shown a strong dependence on the pH values. Using the values of N_D the depletion layer width can be calculated by equation 1.10 that clearly shows; the variation in N_D affecting the depletion layer width (W) at the semiconductor/electrolyte interface.

$$W = \left(\frac{2\varepsilon_1\varepsilon_0}{eN_D}\right)^{\frac{1}{2}}\left(V - V_{fb} - \frac{K_bT}{e}\right)^{\frac{1}{2}} \quad (1.10)$$

The thinnest depletion region was obtained in pH 12 (Table 2), resulting a higher mobility of the charge carriers. Therefore, we may suggest that at pH 12 improved photogenerated carriers separation is obtained thereby; enhancing the PEC activity.[51,52] For an n-type semiconductor when negative biasing is applied the band bending decreases. For higher negative biasing a blocking potential is obtained when depletion region is absent or more likely, the semiconductor responds like a metal, once the Helmholtz layer dominates the interface and the system exhibits a lack of electrochemical dependence on light. At that moment the photocurrent onset is achieved and the applied potential is called flat band potential (V_f).[27] It can be seen in Fig. 8, that photocurrent onset i.e V_f strongly depends on the pH. In addition, the values estimated from the photocurrent onset corroborate the values obtained from the Mott-Schottky curves (Fig. 7). The calculated positions of the CBM are listed in Table 2.[53] In addition, the bandgap energy calculated from the difference of the CBM and VBM is found to be 2.1V (Table 2) corroborating the optical bandgap energy obtained by Fig. 4. Interestingly, the positions of the CBM and the VBM determined here for monoclinic thin film match the orthorhombic Ta_3N_5 film.[32] These results show that the band structures of monoclinic and orthorhombic phase of Ta_3N_5 do not differ from each other. To elucidate the mechanism of charge carriers recombination at different pHs, V_{oc} measurements were performed (Fig. 9a). The system was left under dark to achieve steady state equilibrium. At this state, the Fermi level is the same on both sides of the interface and the resulting voltage difference is the V_{oc}. It can be seen that the V_{oc} under dark shifts negatively from acidic to alkaline electrolyte (Table 2).

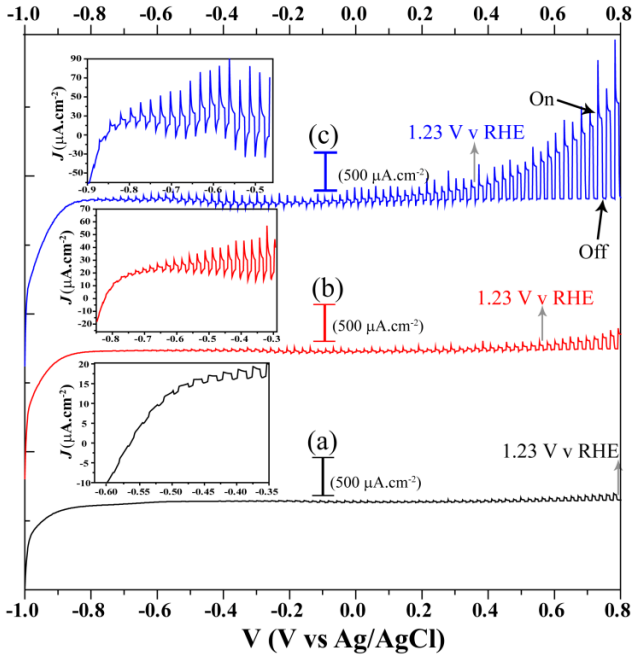

Fig. 8 Chopped LSV curves obtained in 0.1 M phosphate buffer solutions adjusted to pH (a) 4 (b) 8 and (c) 12.

Under illumination the steady state equilibrium is perturbed, once the Fermi level of the semiconductor rises toward the flat band.[30] The photogenerated holes are scavenged by the electrolyte species and electrons will start accumulating on the semiconductor. As a result the V_{oc} will rise until the accumulation is saturated and new equilibrium state is achieved.[51] Fig. 9 shows that under illumination (1 Sun) the V_{oc} shifts ca. 0.25 V toward the negative potentials, for all electrolytes. These results show that the pH of the electrolyte has no effect on the shift of the band bending caused by a constant illumination on Ta_3N_5 thin films.

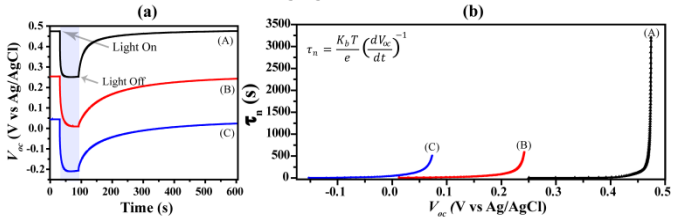

Fig. 9 (a) Open circuit decay and (b) electron recombination lifetime. The measurements were performed in 0.1 M sodium phosphate buffer solutions adjusted to pH (A) 4, (B) 8 and (C) 12.

Using a previously reported method we have calculated the τ_n as a function of V_{oc} decay by equation 1.11:[54]

$$\tau_n = \frac{K_b T}{e}\left(\frac{dV_{oc}}{dt}\right)^{-1} \qquad (1.11)$$

Once the new equilibrium is achieved under illumination, the light is chopped off and the system is left to return the steady state under dark. The accumulated electrons recombine with the holes as a result V_{oc} decays. Monitoring that decay provides kinetic insight of the electron recombination lifetime (τ_n).

Compared to the electrolytes at pH 8 and 12, the lifetime obtained for pH 4 is significantly longer (Fig. 9b). Surface traps play an important role for the electron accumulation and transportation through the semiconductor film. The trap mediated recombination is slower than the direct electron-hole recombination.[55] Therefore, we may consider that the monoclinic Ta_3N_5 thin films in acidic conditions exhibit more contributions from trapping and detrapping of the electron, due to surface states.

Combining the results presented in Table 2 we have constructed the energy level diagram of monoclinic Ta_3N_5 thin films, under dark and illumination (Fig. 10). The band structure of monoclinic Ta_3N_5 thin films straddles the water oxidation/reduction potentials, however, V_f of Ta_3N_5 is very close to the water reduction potential, which might be a reason for lower PEC activity from pristine Ta_3N_5.

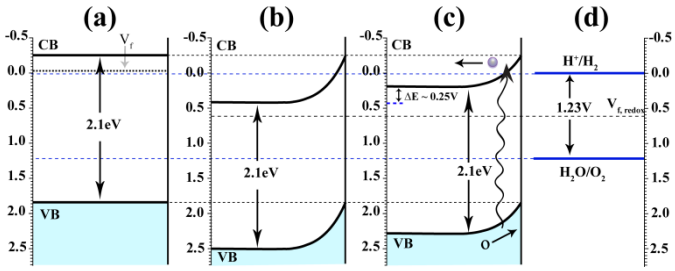

Fig. 10 Schematic illustration of the energy level diagram of monoclinic Ta_3N_5 thin films; (a) Before immersion in electrolyte, (b) at steady state under dark, (c) at equilibrium under illumination (1 Sun) and (d) redox potentials of water splitting. The diagram is to the scale and potentials are shown vs RHE.
V_f and $V_{f,\,redox}$ represent the flat band of Ta_3N_5 thin films and Fermi level of H_2O, respectively.

Earlier reports in the literature have shown that pre-doping a semiconductor shifts up the flat band improving the PEC performance and further enhancement can be achieved by post-loading a suitable co-catalyst.[1,52] Therefore, doping the monoclinic Ta_3N_5 and loading a suitable co-catalyst would be an interesting approach to improve the PEC activity.

Conclusions

In summary, we have synthesized monoclinic Ta_3N_5 thin films by thermal nitridation of Ta_2O_5 directly deposited by RF-magnetron sputtering. Thermal nitridation triggers nitrogen and tantalum Schottky defects and substitutional oxygen in 3-coordinated N atoms. The surface of the monoclinic Ta_3N_5 thin film was found to present different chemical composition compared to the underlying film. Real ε_1 and imaginary ε_2 parts of dielectric functions of the monoclinic Ta_3N_5 were analyzed by the SE within a broad spectral range of 0.54–4.6 eV. The optical parameterization of SE data was carried out using the Tauc-Lorentz and Lorentz oscillators. Concerning the application of the material in PEC water splitting, the dielectric constant ε_1 of Ta_3N_5 film in the visible spectral region (3.1–1.7 eV) was found within the range of 7–9. The PEC analyses revealed that the band structure of Ta_3N_5 is strongly influenced by the

pH of the electrolyte. The enhanced photocurrent obtained from the monoclinic Ta_3N_5 is attributed to the shorter depletion region width and the lower recombination life time in alkaline conditions. The structural insight of the monoclinic Ta_3N_5 thin films, the knowledge of the dielectric constant, the light absorption depth and the band structure is a forward step towards a better understanding of the material and the tailoring of efficient semiconductors for water splitting.

Experimental

Thin Films Fabrication

Prior to the film deposition, quartz, Si and Ti substrates were cleaned by sequential sonication for 30 min each in detergent mixed distilled water and isopropyl alcohol, rinsed with water and then dried under nitrogen flux. Thin films of Ta_2O_5 were sputtered on the substrates by using RF Magnetron sputtering (AJA ORION, 8) technique. The sputtering target consisted of 50.8 mm (2.0 in) diameter Ta_2O_5 (99.95% purity, AJA International, Inc). The base pressure of the sputtering chamber was 3.2×10^{-11} mbar. The argon flow rate was 20 sccm such that the chamber pressure was maintained at 2.6×10^{-3} mbar during the sputtering process. The substrate temperature was kept 21°C and RF power of 150 W with DC self-bias voltage around 2–10 V was used for deposition. The distance between the target and substrate was kept to be 14.7 cm and the substrate holder was rotated to a frequency of 20 rpm. Before deposition process, a pre-sputtering of 5 min was made to clean the target and afterwards, the films were deposited for a deposition time of 300 min. The sputtering rate was 3 nm min^{-1}. The as-deposited Ta_2O_5 films were transformed to Ta_3N_5 films by heating at 900°C for 24 h in a tube oven. A special gas mixture of NH_3 : Ar in a volume ratio of (1:9) was used as a reaction gas. The flux of the gas was kept as 100 ml min^{-1}. The heating and cooling rates of the oven were kept constant (5° C min^{-1}).

Thin Films Characterization

Ta_3N_5 samples sputtered over the quartz substrate were used for all characterizations except for PEC measurements. Scanning Electron Microscopy (SEM) was performed using an EVO 50 from Zeiss, operated at 10 kV. For High resolution transmission microscopy (HRTEM) and selected area electron diffraction (SAED), the samples were prepared in plan view and analysed by JEOL JEM 2010 microscope. Chemical composition of the surface was studied by X-ray photoelectron spectroscopy (XPS) performed in an Omicron-SPHERA station using Al Kα radiation (1486.6 eV) equipped with sputter etching ion gun. The anode was operated at 225 W (15 kV, 15 mA). Survey spectra were recorded with 50 eV pass energy. The Ta 4f, N1s and O1s regions were recorded with a higher resolution (pass energy of 10 eV). Energy scale of the XPS spectra was corrected using the binding energy of advantageous carbon (C1s = 284.6 eV). The detection angle of the photoelectrons (Θ) with respect to the sample surface (take-off angle) was fixed at 53° for all measurements. The depth profile of T_3N_5 thin film was obtained by sputter etching; that was performed at 5 keV Ar^+ ions for a time of 6h.

Rietveld refinements

X-ray Diffraction (XRD) was performed by D500 diffractometer from Siemens. Graphite monochromator was used and the XRD patterns were recorded for a 2θ range from 10° to 90° with a step of 0.05° and measurement time of 5 s per step with Cu K_α radiation (λ = 1.54 Å). Data processing was performed by the Rietveld method using FullProf software.[56] The instrumental resolution function (IRF) of the diffractometer was obtained using LaB_6 standard. The pseudo-Voigt profile function of Thompson, Cox and Hastings was used with an asymmetry correction at low angles.[57] Corrections to the preferred orientation were performed using the Modified March's function.[58,59,60] The grain size has been calculated by modified Scherrer equation (1.1) considering the microstrain as minimum as possible.

$$\beta_h = \frac{\lambda}{D_h \cos\theta} = \frac{\lambda}{\cos\theta} \sum_{lmp} a_{lmp}\, y_{lmp}(\theta_h, \Phi_h) \qquad (1.1)$$

where β_h is the size contribution to the integral breadth of reflection. h and y_{lmp} are the normalized real spherical harmonics.[61] The arguments are the polar angles of the vector h with respect to the Cartesian crystallographic frame. After refinement of the coefficients the program calculates the apparent size (in angstroms Å) along each reciprocal lattice vectors if the IRF is provided in a separate file. The preferential orientation has been identified by using the modified March´s function:

$$P_h = G_2 + (1 - G_2)\left((G_1 cos\alpha_h)^2 + \frac{sin^2\alpha_h}{G_1}\right)^{-3/2} \qquad (1.2)$$

where G_1 corresponds to the Bragg−Brentano geometry, G_2 represents the fraction of the sample without orientation, and α_h is the acute angle between the scattering vector and the normal to the crystallites. The anisotropic size broadening effects, related to the coherence volume of diffraction, were simulated using a model of spherical harmonics.[56]

Optical measurements

The UV-Vis transmittance (T) and reflectance (R) (Fig. S1†) were obtained using standard integrating sphere accessory in Agilent CARY 5000 spectrophotometer in the spectral range of 200–8 00 nm. From the experimental T and R data we have determined the absorption coefficient (α) following previously described method by equation:[15]

$$\alpha = \frac{1}{t} ln\left(\frac{1-R}{T}\right) \qquad (1.3)$$

where t is the thickness of the film. The thickness of the film was measured by profilometry using AMBIOS XP 2 profilometer. Transmittance spectrum shown in Fig. S7† was measured by Jasco V-570 (Japan) spectrophotometer in the spectral range of 300–2 300 nm with a step of 2 nm. Variable angle spectroscopic ellipsometry (VASE) was employed to determine the real ε_1 and imaginary ε_2 parts of the dielectric

function of monoclinic Ta_3N_5 films. The SE measurements were performed by VASE® ellipsometer, J.A.Woollam Co., Inc. with automatic rotating analyzer. The ellipsometric parameters Ψ and Δ describing the amplitude ratio and phase difference between p- and s-polarized light waves[28] were measured in the spectral range of 4.60–0.54 eV (270–2 300 nm) with a spectral step of 0.05 eV and angles of light incidence at 50°, 55°, 60°, 65° and 70°. The ellipsometer was equipped with the Auto Retarder® allowing to measure Δ parameter at 360° interval. The software V.A.S.E. for Windows, version 3.768, J.A.Woollam Co., Inc. was used for data fitting, where the fitting was carried out on the basis of iterative Marquardt-Levenberg algorithm. The quality of the model fit to experimental Ψ and Δ was estimated by the mean square error (MSE) function. MSE value close to ≈1 represents a good fit. For the measurements of the optical constants of monoclinic Ta_3N_5 thin films firstly, the SE of pure substrate was measured to find its optical constants and to distinguish them from the thin film. The refractive index of the glass substrate in the spectral range of 270–2 300 nm was evaluated using the Sellmeier equation. The extinction coefficient in this region was $k \approx 0$.

Photoelectrochemical (PEC) measurements

Four types of samples were prepared using different substrates; Ta_3N_5/Pt/Ti/quartz, Ta_3N_5/Pt/Ti/Si, Ta_3N_5/Pt/Ti/SiO_2/Si and Ta_3N_5/Pt/Ti. Ti and Pt were deposited by DC Magnetron sputtering whereas SiO_2 was thermally grown on Si wafer under controlled oxygen flux. The thickness of Pt, Ti and SiO_2 layers was, 200, 7.2 and 150 nm, respectively. Ti layer helped for the adhesion and Pt served as electric contact.[24] Prior to each measurement the samples were etched to possibly clean the surface by HF/H_2O droplets on Ta_3N_5 part of the film. The wires and the exposed conductive parts of the samples were sealed with an epoxy adhesive. We found that the using variety of substrates do not influence the PEC results; therefore, in this work we have applied Ta_3N_5/Pt/Ti/quartz for the measurements.

The photoelectrochemical measurements were performed in a three electrode configuration employing Ta_3N_5/Pt/Ti/quartz as working electrode, Pt wire as counter electrode and Ag/AgCl as a reference electrode. 0.1 M sodium phosphate buffer solutions adjusted to pH 4, 8 and 12 were used. The potentials of the working electrode were controlled by using Auto-lab (AUT 84503). AM 1.5 filter was used to simulate the solar spectrum. The light intensity was calibrated using a silicon photodiode with known responsivity of 100 mW.cm-2 (1 Sun). Linear sweep voltammetry (LSV) curves were obtained at a scan rate of 10 mV/s. The Mott-Shottky plots were obtained at a frequency of 1k Hz with 10 mV of the signal amplitude for a range of applied potentials. The measured potential versus Ag/AgCl was converted to the RHE scale by:

$$V_{RHE} = V_{Ag/AgCl} + (0.059) \times pH + 0.0197\ V$$

Acknowledgements

The authors are grateful for financial support from the following Brazilian agencies: Conselho Nacional de Desenvolvimento Científico e Tecnológico (Processo: 490221/2012-2, 477804/2011-0, 304716/2013-8 and 472243/2013-6). Thanks are due to Dr. Ricardo Rego Correia for his useful discussion on optics, Dr. Claudio Radtke for the XPS measurements, Dr. Pedro Migowski for discussion on chemistry and Dr. Antonio Marcos Helgueira de Andrade for Ta_2O_5 films sputtering.

References

1 Y. Li, L. Zhang, A. Torres-Pardo, J. M. Gonzalez-Calbet, Y. Ma, P. Oleynikov, O. Terasaki, S. Asahina, M. Shima, D. Cha, L. Zhao, K. Takanabe, J. Kubota and K. Domen, *Nat. Commun.*, 2013, **4,** 1.

2 Y. C. Wang, C. Y. Chang, T. F. Yeh, Y. L. Lee and H. Teng, *J. Mater. Chem. A*, 2014, **2**, 2057.

3 S. Khan, M. J. M. Zapata, D. L. Baptista, R. V. Gonçalves, J. A. Fernandes, J. Dupont, M. J. L. Santos and S. R. Teixeira, *J. Phys. Chem. C*, 2015, (**DOI:** 10.1021/acs.jpcc.5b05475).

4 R. V. Goncalves, P. Migowski, H. Wender, A. F. Feil, M. J. M. Zapata, S. Khan, F. Bernardi, G. M. Azevedo and S. R. Teixeira, *CrystEngComm*, 2014, **16**, 797.

5 Y. Moriya, T. Takata and K. Domen, *Coord. Chem. Rev.*, 2013, **257**, 1957.

6 K. Sivula, F. Le Formal and M. Grätzel, *ChemSusChem*, 2011, **4**, 432.

7 B. Klahr, S. Gimenez, F. Fabregat-Santiago, J. Bisquert and T. W. Hamann, *Energ. Environ. Sci.*, 2012, **5**, 7626.

8 Q. H. Zhang and L. Gao, *Langmuir*, 2004, **20**, 9821.

9 Z. Wang, J. G. Hou, C. Yang, S. Q. Jiao, K. Huang and H. M. Zhu, *Energ. Environ. Sci.*, 2013, **6**, 2134.

10 N. E. Brese, M. Okeeffe, P. Rauch and F. J. Disalvo, *Acta Crystallogr. Sect. C-Cryst. Struct. Commun.* 1991, **47**, 2291.

11 B. A. Pinaud, A. Vailionis and T. F. Jaramillo, *Chem. Mater.*, 2014, **26**, 1576.

12 N. Terao, CR. Acad. Sci. B Phys., 1977, **285**, 17.

13 S. J. Henderson and A. L. Hector, *J. Solid State Chem.*, 2006, **179**, 3518.

14 J. Wang, J. Feng, L. Zhang, Z. Li and Z. Zou, *Phys. Chem. Chem. Phys.*, 2014, **16**, 15375.

15 A. Ziani, E. Nurlaela, D. S. Dhawale, D. A. Silva, E. Alarousu, O. F. Mohammed and K. Takanabe, *Phys. Chem. Chem. Phys.*, 2015, **17**, 2670.

16 J. J. Wang, T. Fang, L. Zhang, J. Y. Feng, Z. S. Li and Z. G. Zou, *J. Catal.*, 2014, **309**, 291.

17 B. Klahr, S. Gimenez, F. Fabregat-Santiago, J. Bisquert and T. W. Hamann, *Energ. Environ. Sci.*, 2012, **5**, 7626.

18 B. Klahr, S. Gimenez, F. Fabregat-Santiago, T. Hamann and J. Bisquert, *J. Am. Chem. Soc.*, 2012, **134**, 4294.

19 X. Peng, L. Peng, C. Wu and Y. Xie, *Chem. Soc. Rev.*, 2014, **43**, 3303.

20 K. Ariga, Y. Yamauchi, G. Rydzek, Q. Ji, Y. Yonamine, K. C. W. Wu and J. P. Hill, *Chem. Lett.*, 2014, **43**, 36.

21 S. Qiu, M. Xue and G. Zhu, *Chem. Soc. Rev.*, 2014, **43**, 6116.

22 J. A. Fernandes, P. Migowski, Z. Fabrim, A. F. Feil, G. Rosa, S. Khan, G. J. Machado, P. F. P. Fichtner, S. R. Teixeira, M. J.

L. Santos and J. Dupont, *Phys. Chem. Chem. Phys.*, 2014, **16,** 9148**.**
23 M. P. Languer, F. R. Scheffer, A. F. Feil, D. L. Baptista, P. Migowski, G. J. Machado, D. P. de Moraes, J. Dupont, S. R. Teixeira and D. E. Weibel, *Int. J. Hydrog. Energy*, 2013, **38**, 14440.
24 A. Dabirian and R. van de Krol, *Appl. Phys. Lett.*, 2013, **102** 033905.
25 D. Yokoyama, H. Hashiguchi, K. Maeda, T. Minegishi, T. Takata, R. Abe, J. Kubota and K. Domen, *Thin Solid Films*, 2011, **519**, 2087.
26 Y. Q. Cong, H. S. Park, S. J. Wang, H. X. Dang, F. R. F. Fan, C. B. Mullins and A. J. Bard, *J. Phys. Chem. C*, 2012, **116**, 14541.
27 R. Beranek, *Advances in Physical Chemistry*, 2011, **2011**, 1.
28 K.H. Zaininger and A. G. Revesz, *RCA Rev.* , 1964, **25**, 85.
29 M. S. M. Courdille, J.B. Thesten,, *Journal*, 1980, **80**, 20838.
30 A. J. Nozik and R. Memming, *The Journal of Physical Chemistry*, 1996, **100**, 13061.
31 S. H. Mohamed, O. Kappertz, T. Niemeier, R. Drese, M. M. Wakkad and M. Wuttig, *Thin Solid Films*, 2004, **468**, 48.
32 W. J. Chun, A. Ishikawa, H. Fujisawa, T. Takata, J. N. Kondo, M. Hara, M. Kawai, Y. Matsumoto and K. Domen, *J. Phys. Chem. B.*, 2003, **107**, 1798.
33 C. T. Satoshi Hashimoto, Aki Murata, and Tsuguo Sakurada, *J. Surf. Anal.*, 2006, **13,** 14**.**
34 R. V. Goncalves, R. Wojcieszak, P. M. Uberman, S. R. Teixeira and L. M. Rossi, *Phys. Chem. Chem. Phys.*, 2014, **16**, 5755.
35 W. Feng, G. Chen, L. Li, G. Lv, X. Zhang, E. Niu, C. Liu and S.-Z. Yang, *J. Phys.D: Appl. Phys.s*, 2007, **40**, 4228.
36 M. Li, W. Luo, D. Cao, X. Zhao, Z. Li, T. Yu and Z. Zou, *Angew. Chem. Int. Ed.*, 2013, **52**, 11016.
37 E. Nurlaela, S. Ould-Chikh, M. Harb, S. del Gobbo, M. Aouine, E. Puzenat, P. Sautet, K. Domen, J.-M. Basset and K. Takanabe, *Chem. Mater.*, 2014, **26**, 4812.
38 R. Abe, *J.Photochem. Photobiol. C: Photochem. Rev.*, 2010, **11**, 179.
39 D. E. Aspnes and A. A. Studna, *Phys Rev B*, 1983, **27**, 985.
40 E. Langereis, S. B. S. Heil, H. C. M. Knoops, W. Keuning, M. C. M. v. d. Sanden and W. M. M. Kessels, *J. Phys. D: Appl.Phys.*, 2009, **42**, 073001.
41 J. M. Morbec, I. Narkeviciute, T. F. Jaramillo and G. Galli, *Phys.Rev. B.*, 2014, **90**, 155204.
42 E. Langereis, H. C. M. Knoops, A. J. M. Mackus, F. Roozeboom, M. C. M. van de Sanden and W. M. M. Kessels, *J.Appl. Phys.*, 2007, **102**, 083517.
43 G. E. Jellison and F. A. Modine, *Appl Phys Lett*, 1996, **69**, 2137.
44 G. E. Jellison and F. A. Modine, *Appl. Phys. Lett.*, 1996, **69**, 371.
45 F. Wooten, Optical Properties of Solids (Academic Press, New York, 1972) p.52.
46 C. M. Fang, E. Orhan, G. A. de Wijs, H. T. Hintzen, R. A. de Groot, R. Marchand, J. Y. Saillard and G. de With, *J. Mater. Chem.*, 2001, **11**, 1248.
47 D. A. G. Bruggeman, *Annalen der Physik*, 1935, **416**, 636.
48 C. A. Koval and J. N. Howard, *Chem. Rev.*, 1992, **92**, 411.
49 R. Degryse, W. P. Gomes, F. Cardon and J. Vennik, *J. Electrochem. Soc.*, 1975, **122**, 711.
50 L. Cui, M. Wang and Y. X. Wang, *J.Phys. Soc. Jpn.*, 2014, **83**, 114707.
51 R. G. Freitas, M. A. Santanna and E. C. Pereira, *Electrochim. Acta.*, 2014, **136**, 404.
52 M. J. Liao, J. Y. Feng, W. J. Luo, Z. Q. Wang, J. Y. Zhang, Z. S. Li, T. Yu and Z. G. Zou, *Adv. Funct. Mater.*, 2012, **22**, 3066.
53 Y. Matsumoto, *J. Solid State Chem.*, 1996, **126**, 227.
54 J. Bisquert, A. Zaban, M. Greenshtein and I. Mora-Seró, *J Am. Chem. Soc.*, 2004, **126**, 13550.
55 B. H. Meekins and P. V. Kamat, *Acs Nano.*, 2009, **3**, 3437.
56 J. Rodríguez-Carvajal, *Phys. B: Condens. Matter,* 1993, **192**, 55.
57 P. Thompson, D. E. Cox and J. B. Hastings, *J. Appl. Crystallogr.*, 1987, **20**, 79.
58 W. Dollase, *Appl.Crystallogr.*, 1986, **19**, 267.
59 L. B. McCusker, R. B. Von Dreele, D. E. Cox, D. Louer and P. Scardi, *Appl.Crystallogr.*, 1999, **32**, 36.
60 R. V. Goncalves, P. Migowski, H. Wender, D. Eberhardt, D. E. Weibel, F. C. Sonaglio, M. J. M. Zapata, J. Dupont, A. F. Feil and S. R. Teixeira, *J. Phys. Chem. C*, 2012, **116**, 14022.
61 M. Jarvinen, *J. Appl. Crystallogr.*, 1993, **26**, 525.